Supplementary information for Efficient and cold-tolerant moisture-enabled generator combining ionic diode and ionic hydrogel

Jiahao Fang[1], Xiang Zhang[1], Peng Duan[1], Zhongbao Jiang[1], Xulei Lu[1], Chunqiao Fu[1], Yong Zhang[1], Yuming Yao[1], Kedong Shang[1], Jieyang Qin[1], Yangfan Liu[1], Tingting Yang[1,2]*

[1]Tribology Research Institute, School of Mechanical Engineering, Southwest Jiaotong University, Chengdu 610031, Sichuan, PR China

[2]Institute of Smart City and Intelligent Transportation, Southwest Jiaotong University, Chengdu 610031, Sichuan, PR China

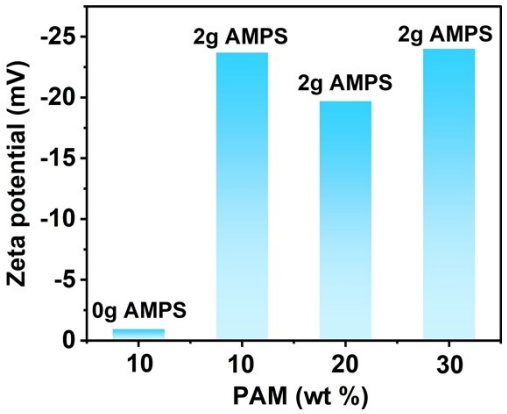

Fig. S1. Zeta potential of hydrogels without AMPS (10 wt% PAM) and with different PAM (2g AMPS) contents.

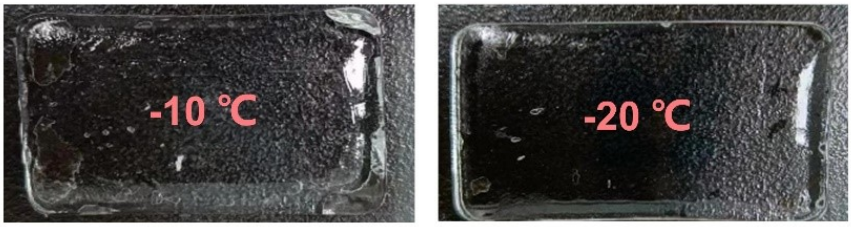

Fig. S2. Photos of ion hydrogel antifreeze.

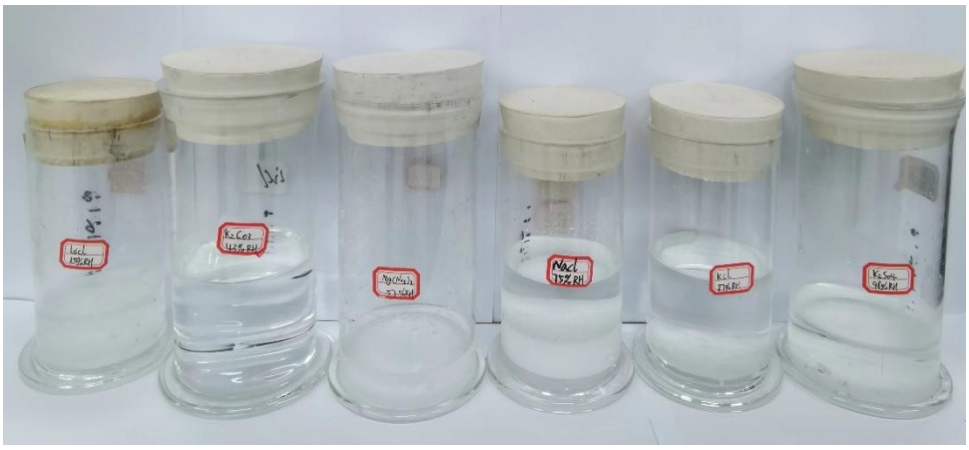

Fig. S3. Humidity values correspond to different saturated salt solutions.

Table S1. Humidity values correspond to different saturated salt solutions.

Salt solution	LiCl	K_2CO_3	$Mg(NO_3)_2$	NaCl	KCl	K_2SO_4
Relative humidity（RH）	15%	43%	57%	75%	87%	98%

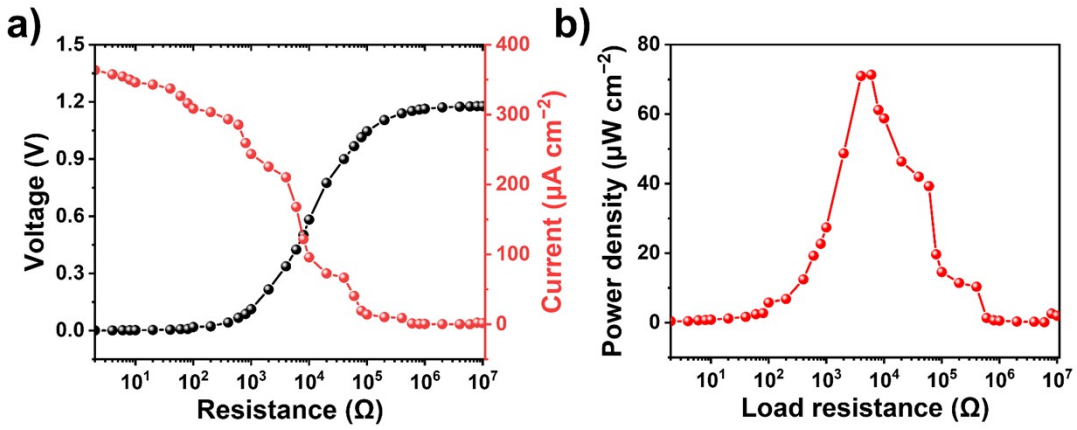

Fig. S4. Variation of device electrical output performance with external load.

Table S2. Comparison of power generation performance.

Material	relative humidity (RH)	V_{OC}	J_{SC} (μA cm^{-2})	Power density (μW cm^{-2})	Reference
HPCNF/AAO/ EGaIn	93%	1.1 V	27	8.5	1

PSSA	80%	0.8 V	100	17	2
GOF	70%	0.7 V	25	18	3
grGO	80%	1.5 V	0.0272	about 0.0045	4
Heterogenous paper	60%	0.78 V	0.83	0.7	5
MAO-MEG	20-95%	0.6 V	1160	24.8	6
TiO2 nanowire networks	85%	0.52 V	8	4	7
PAM/APPS/LiCl-AAO	93%	1.25	300	71.35	This work

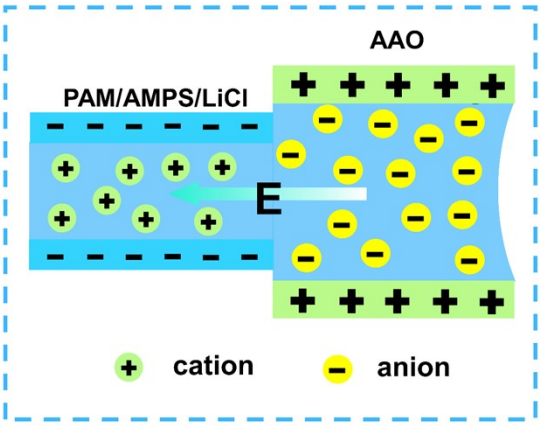

Fig. S5. Schematic diagram of the directional movement of ions.

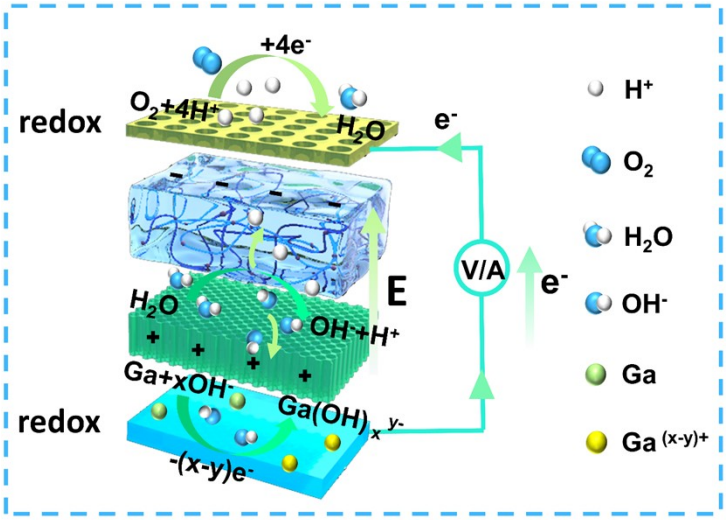

Fig. S6. Schematic diagram of device operation.

Synergistic effects of the hydrovolt effect and redox reactions

First, we believe that the spatial separation of anions and cations is the basis for power generation. To verify the above view, we use negatively charged SiO_2 nanoporous film and uncharged TiO_2 nanoporous film instead of anodic aluminum oxide (AAO, positively charged). The antisymmetric surface polarity of the nanopores is experimentally demonstrated to be a prerequisite for high-performance power generation. Even if the lower electrode is made of active metal, the device still has no power output if the ionic diode structure is not fulfilled and the anion-cation space separation is insufficient (Fig. S7). In addition, we measured the electrical output in a humid (93% RH) environment for devices with various bottom electrode materials, which were ranked in order of activity from high to low, *i.e.*, Al, Zn, C, and Au. The results show that the device performance is positively correlated with the activity of the bottom electrodes, as shown in Fig. S8a. We note that for bottom electrodes with inert metals (*e.g.*, C, Au) there is no redox reaction, and although the current decreases significantly (Fig. S8b), there is still a considerable voltage signal (C ~ 0.45 V, Au ~ 0.46 V). This should be attributed to the result of the directional movement of ions induced by the built-in electric field. Since the spatial separation of ions requires energy, which we believe comes from the hydrovolt effect, it should specifically include the humidity gradient energy and the thermal energy released by the gas-liquid phase transition.

We chose liquid metal as the bottom electrode of the device because it has good wettability, conductivity, and a simple process. Carbon electrode is chosen as the top electrode because its good adhesion and conductivity are favorable for electrode fabrication. Since the built-in electric field driving the ions enriched to the vicinity of the electrode will hinder the migration of subsequent ions, the introduction of an active electrode will deplete the ions in the vicinity of the electrode through redox reactions, clearing the way for the sustained directional transport of subsequent ions. Therefore, we believe that our proposed device is the result of the synergistic work of the hydrovolt effect and the redox reaction. When gold or carbon is used as the lower electrode, it is unable to continuously deplete the ions near the electrode, resulting in a rapid decay of the initial current from Au ~ 28 $\mu A/cm^2$ and C ~ 9 $\mu A/cm^2$ to Au ~ 1.5 $\mu A/cm^2$ and C ~ 0.5 $\mu A/cm^2$, as shown in Fig. S8b.

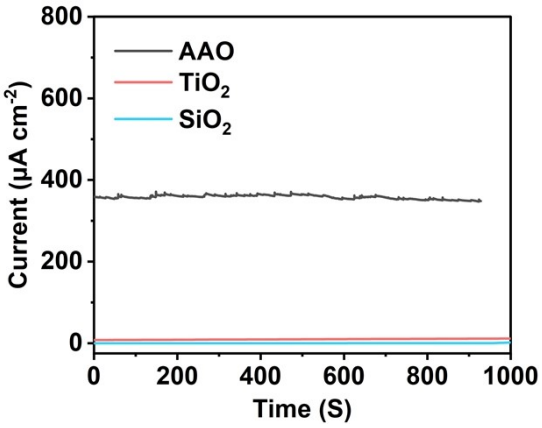

Fig. S7. Current density of the device after substitution of AAO by nanoporous films with different chargeability (SiO_2 negatively charged and TiO_2 uncharged).

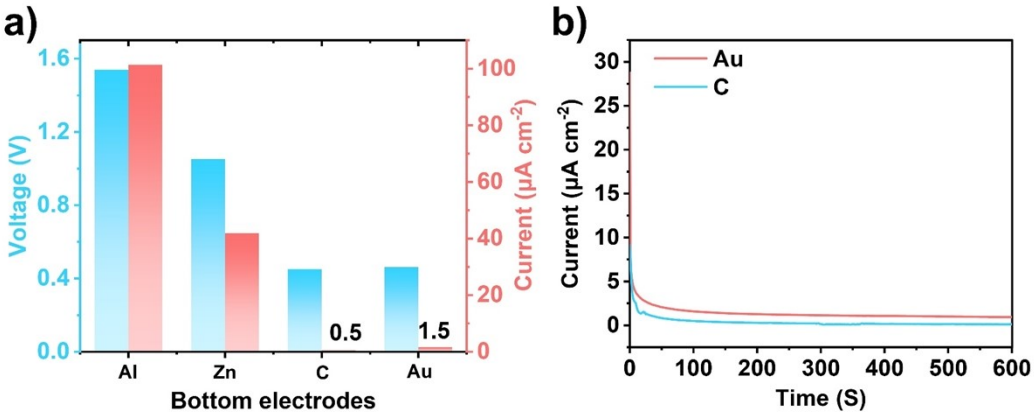

Fig. S8. a) Difference in device performance for different bottom electrodes in high humidity (93% RH) environments. b) Current output of Au and C electrodes.

Numerical Simulation

In order to further illustrate the existence of the rectification effect of the nanofluidic diode, the rectification effect of the device is simulated and analyzed based on the Nernst Planck equation using COMSOL simulation software. The Nernst Planck equation is shown below:

$$j_i = D_i\left(\nabla C_i + \frac{z_i F c_i}{RT}\nabla\varphi\right) \quad (1)$$

$$\nabla^2\varphi = -\frac{F}{\varepsilon}\sum z_i c_i \tag{2}$$

$$\nabla j_i = 0 \tag{3}$$

In the equations, j_i, D_i, C_i, and φ are the ion flux, diffusion coefficient, ion concentration, and potential, respectively; R, F, T, and ε are the universal gas constant, Faraday's constant, absolute temperature, and dielectric constant of the electrolyte solution, respectively. The simulation model used for PAM/AMPS/LiCl-AAO is shown in Fig. S9.

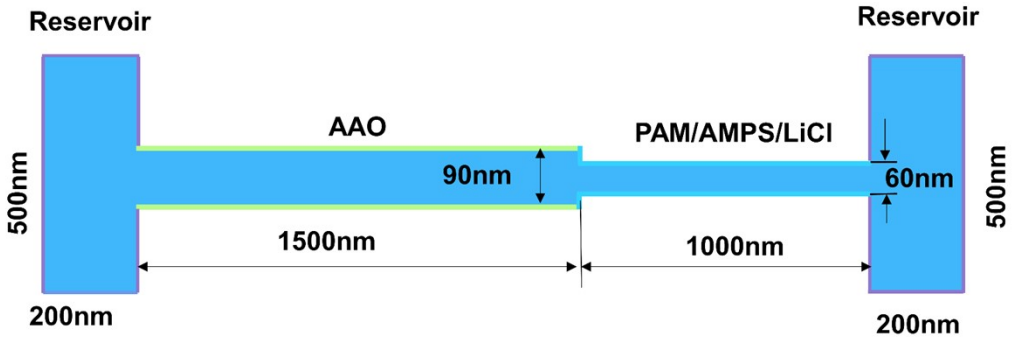

Fig. S9. A numerical simulation model based on PNP theory.

The transmembrane transport of ions in membranes is thought to be controlled by the surface charge in the nano-channels. In the COMSOL simulations, PAM/AMPS/LiCl was idealized as a cylindrical tube with a pore diameter of 60 nm and a length of 1000 nm for simulation purposes, while AAO was modeled as a cylindrical tube with a channel diameter of about 90 nm and a length of 1500 nm. The pore surface charge densities of PAM/AMPS/LiCl and AAO were set to $-1.5e^{-4}$ and $1e^{-4}$ C/m^2, respectively. In order to simulate the humidity conditions in the real environment, two water reservoirs with dimensions of 200 × 500 nm were introduced to set up the actual environment in COMSOL, and the water environment was also set up in the pores of PAM/AMPS/LiCl and AAO. The surface charge density of the reservoirs was set to 0 C m^{-2}. The initial concentration of mobile ions (Li^+ and Cl^-) in the PAM/AMPS/LiCl orifices was set to 10^{-6}M.

Suppose that our system can be explained quantitatively by Poisson and energy-Planck equations with appropriate boundary conditions. The simulated temperature is

298 K and the salt solution has a dielectric constant of 70. The ion flux at the boundary satisfies the conditions:

$$\vec{n} \cdot j_i = 0 \qquad (4)$$

The boundary condition for the potential on the channel walls reads

$$\vec{n} \cdot \nabla_{\varphi} = -\frac{\sigma}{\varepsilon} \qquad (5)$$

Where σ represents the channel wall surface charge density.

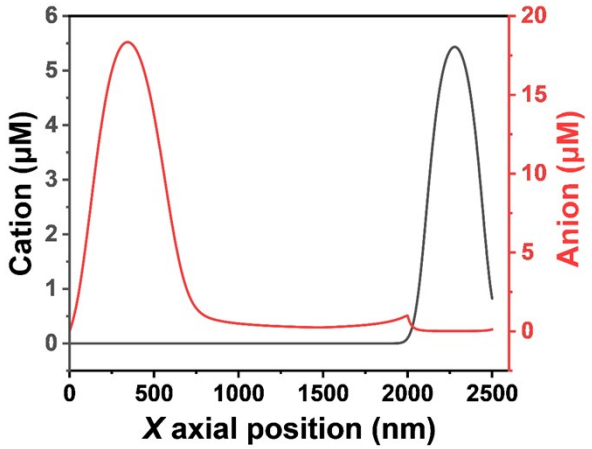

Fig. S10. Distribution of anions and cations in nano-channels.

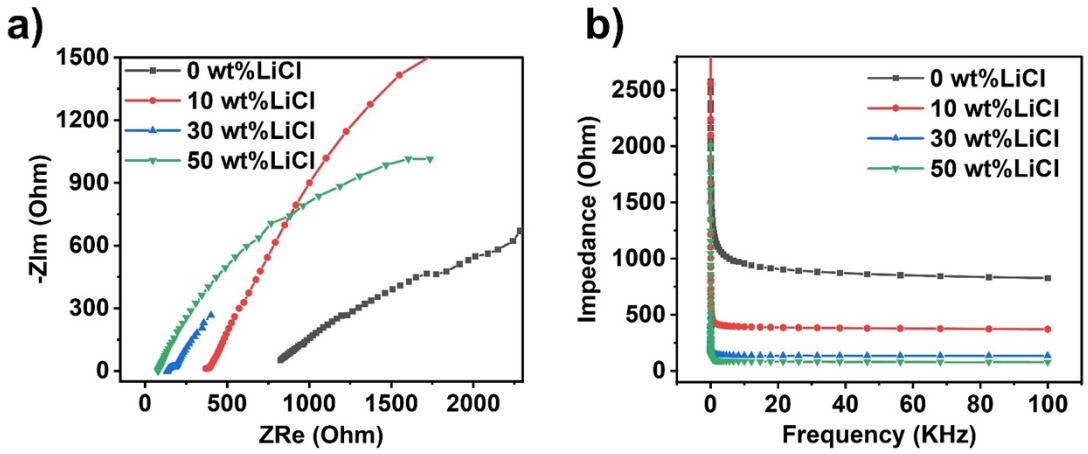

Fig. S11. impedance of devices treated with different weights (0 wt%, 10 wt%, 30 wt%, 50 wt%) of LiCl. a) Impedance spectra of devices treated with different weights of LiCl. b) Impedance versus frequency curves of devices treated with different weights of LiCl.

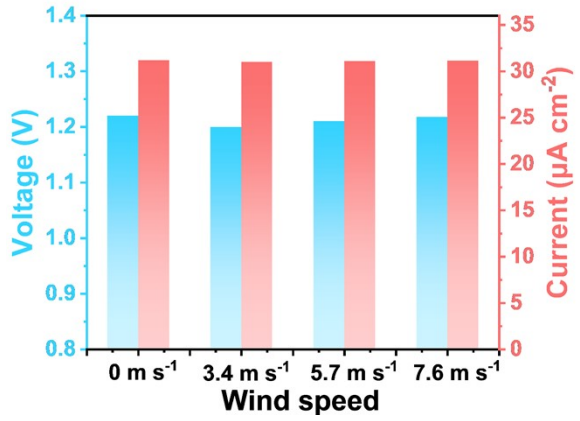

Fig. S12. Effect of wind speed on the device's open-circuit voltage and short-circuit current.

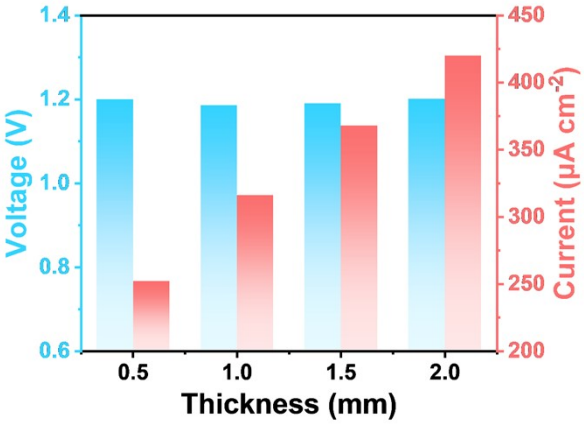

Fig. S13. Effect of ionic hydrogel film thickness on devices' open-circuit voltage and short-circuit current.

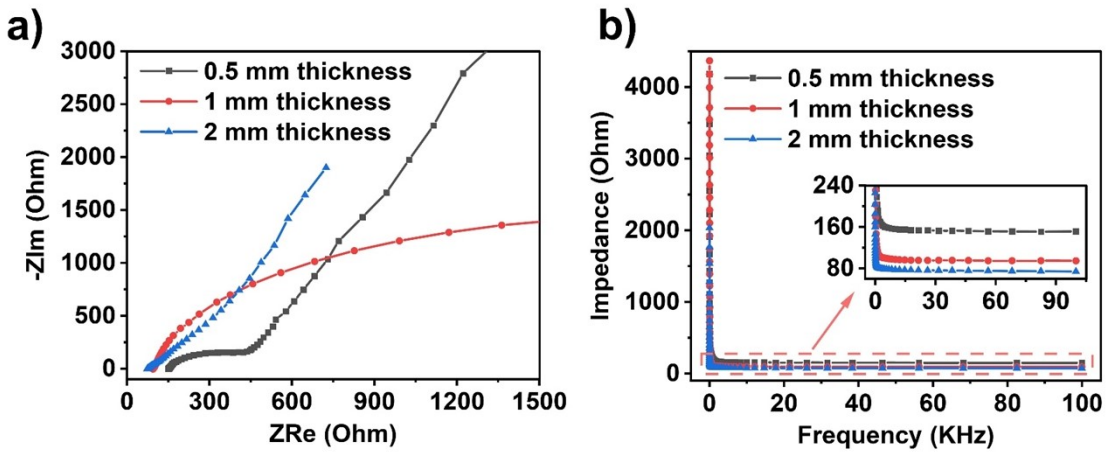

Fig. S14. Impedance of devices prepared with different thicknesses (0.5 mm, 1 mm, 2 mm) of hydrogels. a) Impedance spectra of devices prepared with different thicknesses

of hydrogels. b) Variation curves of impedance with frequency of devices prepared with different thicknesses of hydrogels.

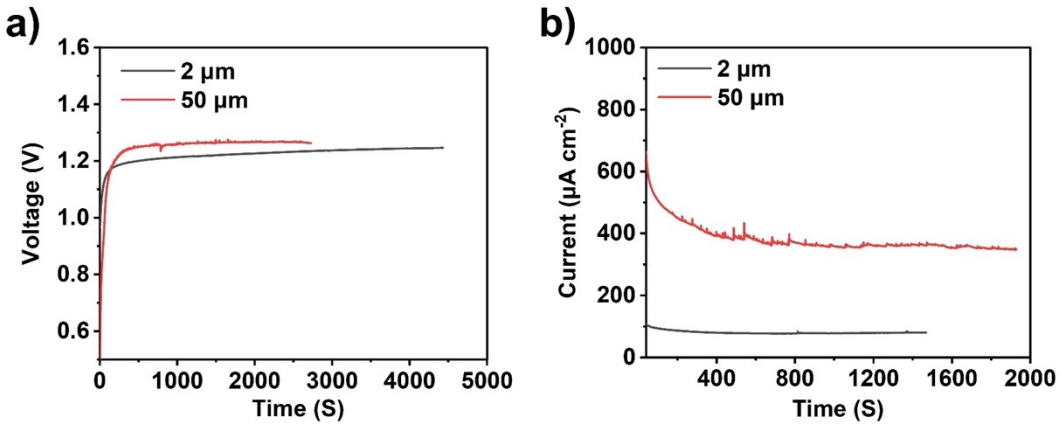

Fig. S15. Effect of different carbon electrode thicknesses on device output a) current and b) voltage.

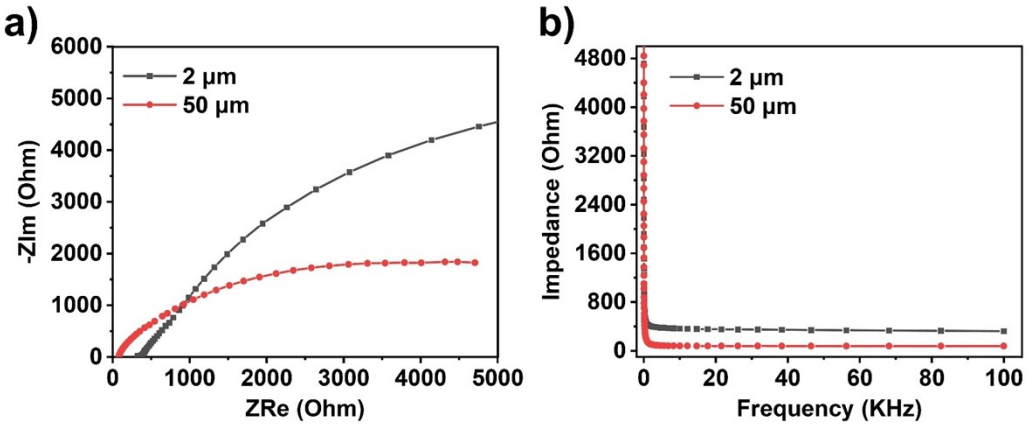

Fig. S16. Impedance of devices prepared with different thicknesses (2 μm, 50 μm) of carbon electrodes. a) Impedance spectra. b) Impedance versus frequency curves.

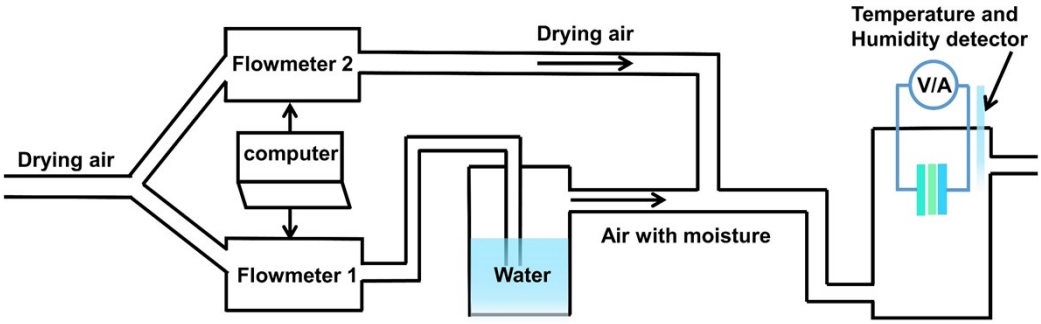

Fig. S17. Schematic diagram of the principle of humidity control by the bubble method.

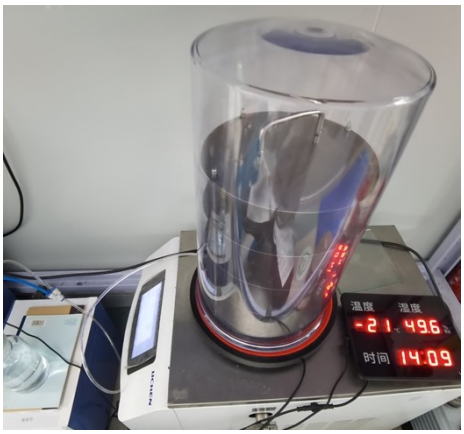

Fig. S18. -20°C, 50% RH control of environmental conditions.

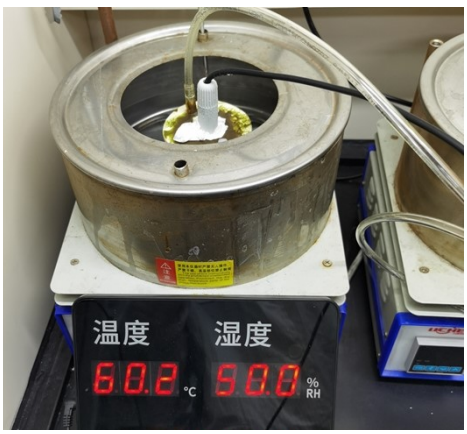

Fig. S19. Control of environmental conditions at 60°C, 50% RH.

References

1. X. Lu, T. Yang, C. Fu, Z. Jiang, Y. Zhang, K. Shang, C. He, J. Zhou and Q. C. He, *Advanced Energy Materials*, 2022, **12**, 2202634.
2. T. Xu, X. Ding, Y. Huang, C. Shao, L. Song, X. Gao, Z. Zhang and L. Qu, *Energy & Environmental Science*, 2019, **12**, 972-978.
3. T. Xu, X. Ding, C. Shao, L. Song, T. Lin, X. Gao, J. Xue, Z. Zhang and L. Qu, *Small*, 2018, **14**, 1704473.
4. Y. Huang, H. Cheng, C. Yang, P. Zhang, Q. Liao, H. Yao, G. Shi and L. Qu, *Nature Communications*, 2018, **9**, 4166.
5. J. Tan, S. Fang, Z. Zhang, J. Yin, L. Li, X. Wang and W. Guo, *Nature Communications*, 2022, **13**, 3643.
6. K. Zhao, J. W. Lee, Z. G. Yu, W. Jiang, J. W. Oh, G. Kim, H. Han, Y. Kim, K. Lee and S. Lee, *ACS nano*, 2023, **17**, 5472-5485.
7. D. Shen, M. Xiao, G. Zou, L. Liu, W. W. Duley and Y. N. Zhou, *Advanced Materials*, 2018, **30**, 1705925.